Green Chemistry

PAPER

View Article Online
View Journal

Cite this: DOI: 10.1039/d5gc01937k

Crystal phase engineering and surface reconstruction in Co–Mn phosphides: unraveling the mechanisms of high-performance water oxidation catalysis†

Tingting Tang,[a] Yanfang Teng,[a] Kuoteng Sun,[c] Yanhan Liu,[a] Zhendong Gao,[a] Tayirjan Taylor Isimjan,[b] Jingya Guo,*[a] Jianniao Tian *[a] and Xiulin Yang *[a]

Crystalline and amorphous catalysts offer disparate advantages in reducing the overpotential of the oxygen evolution reaction (OER). Crystalline phases provide excellent electrical conductivity, while amorphous phases offer abundant unsaturated active sites. This study explores a synergistic strategy that integrates these benefits to develop high-performance OER catalysts with enhanced activity and stability. By employing controlled annealing followed by phosphating, we engineered a transition from low-crystallinity MnP–Co_3P/NF to high-crystallinity MnP–$Co_3(PO_4)_2$/NF, effectively tuning the balance between conductivity and active site availability. Advanced spectroscopic characterization studies (including X-ray photoelectron spectroscopy (XPS), zeta potential analysis, ultraviolet photoelectron spectroscopy (UPS) and electrochemical measurements) reveal that the high-crystallinity MnP–$Co_3(PO_4)_2$/NF catalyst exhibits superior hydrophilicity, an enriched concentration of phosphorus vacancies, and enhanced charge redistribution, collectively leading to significantly improved OER kinetics. The catalyst achieved low overpotentials of 281 mV at 50 mA cm^{-2} and 306 mV at 100 mA cm^{-2}, with exceptional stability for 230 h at 100 mA cm^{-2}, outperforming comparable systems and commercial noble metal catalysts. *In situ* studies revealed faster formation of the active CoOOH phase on high-crystallinity MnP–$Co_3(PO_4)_2$/NF. This work provides valuable insights into designing efficient and durable OER catalysts for energy conversion applications.

Received 17th April 2025,
Accepted 19th June 2025

DOI: 10.1039/d5gc01937k

rsc.li/greenchem

Green foundation

1. A crystalline–amorphous MnP–$Co_3(PO_4)_2$/NF catalyst, engineered through controlled annealing and phosphating, combines high electrical conductivity with abundant active sites, delivering outstanding OER performance and enabling efficient green hydrogen production.
2. The catalyst achieves record-low overpotentials (281/306 mV at 50/100 mA cm^{-2}) and exceptional long-term stability over 230 hours, outperforming noble-metal benchmarks. In full electrolyzers, it delivers high current densities (200–1000 mA cm^{-2}) at lower operating voltages (1.80–2.02 V), surpassing commercial RuO_2‖Pt/C systems.
3. Advanced characterization confirms that MnP–$Co_3(PO_4)_2$/NF enhances OER kinetics *via* improved hydrophilicity, abundant P vacancies, and optimized charge redistribution. Future research should prioritize mild-temperature/renewable-energy synthesis, metal recycling, and life cycle assessment to boost eco-efficiency and enable scalable green hydrogen production.

1. Introduction

Electrocatalytic water splitting is a pivotal technology for advancing the hydrogen economy and enabling green hydrogen production, offering a sustainable pathway to address environmental challenges.[1,2] However, its practical industrial application is constrained by low energy conversion efficiency, primarily due to the multistep proton–electron transfer process in the oxygen evolution reaction (OER) and the formation of O–O bonds, which result in sluggish reaction kine-

[a]*Guangxi Key Laboratory of Low Carbon Energy Materials, School of Chemistry and Pharmaceutical Sciences, Guangxi Normal University, Guilin 541004, China. E-mail: xlyang@gxnu.edu.cn, jyguo@gxnu.edu.cn, birdtjn@sina.com*
[b]*Saudi Arabia Basic Industries Corporation (SABIC) at King Abdullah University of Science and Technology (KAUST), Thuwal 23955-6900, Saudi Arabia*
[c]*Liuzhou Bureau of EHV Transmission Company of China Southern Power Grid Co. Ltd, Liuzhou 545006, China*

† Electronic supplementary information (ESI) available. See DOI: https://doi.org/10.1039/d5gc01937k

tics.[3] This highlights the urgent need for innovative OER catalyst design to enable scalable and efficient water-splitting technologies. Noble metal oxides such as IrO_2 and RuO_2 are considered state-of-the-art OER catalysts.[4–8] Their scarcity and high cost drive the need for Earth-abundant, cost-effective alternatives. In non-noble metal OER catalyst systems, transition metal-based materials, represented by Co, Fe, Ni, and Mn, have emerged as ideal anode materials for alkaline electrolyzers due to their unique electronic configurations, abundance, and affordability, which make them promising candidates.[9–13]

Transition metal electrocatalysts, especially Mn–Co-based systems, are promising alternatives for the OER due to their tunable electronic structure, abundance, and low cost. In recent years, significant advancements have been made in Mn–Co-based electrocatalysts for the OER, primarily driven by three strategic approaches: (1) electronic structure modulation – Mn–Co alloying reduces e_g orbital filling, enhancing oxygen intermediate binding;[14–16] (2) lattice oxygen activation – Mn-induced strain weakens metal–oxygen bonds, enabling new reaction pathways;[17,18] and (3) dynamic surface reconstruction – under operating conditions, Mn–Co phosphates transform into active (oxy)hydroxides with retained P-doping, forming metastable interfaces that improve catalytic performance.[19,20]

Highly crystalline structures exhibiting excellent conductivity and stability often suffer from a limited number of active sites due to densely packed basal planes that restrict defect formation, thereby hindering catalytic performance.[9] Conversely, amorphous phases, though rich in defect-driven active sites, typically exhibit poor stability and low electrical conductivity, compromising the charge-transfer kinetics and limiting their practical utility.[21,22] Extensive research efforts have focused on overcoming these limitations by synergistically integrating the superior electrical conductivity of crystalline phases with the abundant active sites of amorphous phases.[23,24] This hybrid strategy aims to simultaneously enhance catalytic activity and stability, advancing the development of efficient electrocatalysts for sustainable energy conversion technologies. Recent advances in engineering strategies, including elemental doping, vacancy engineering, morphology optimization, and surface reconstruction, have shown promise in achieving this balance.[25,26] Shao *et al*. demonstrated that doping transition metal-based hydroxides to form binary or ternary heterostructures effectively integrates both phases, enabling precise modulation of the electronic structure and optimization of intermediate adsorption energies, leading to enhanced catalytic performance.[27] However, using conventional methods, the exact synthesis for dense crystalline–amorphous heterostructures with well-defined phase distribution and interfacial characteristics remains challenging.[28,29] Achieving an optimal balance between amorphous and crystalline phases through innovative synthesis strategies and advanced characterization techniques is crucial for designing high-performance OER electrocatalysts.

In this study, annealing before phosphating modulated the crystallinity of Co–Mn phosphates, transitioning from low-crystallinity MnP–Co_3P/NF to high-crystallinity MnP–$Co_3(PO_4)_2$/NF, as confirmed by X-ray diffraction (XRD), selected area electron diffraction (SAED), and high-resolution transmission electron microscopy (HR-TEM). This approach successfully balanced the crystalline and amorphous phases, optimizing the structural and electronic properties. MnP–$Co_3(PO_4)_2$/NF exhibited enhanced hydrophilicity, a higher oxygen vacancy density, and a larger surface area than MnP–Co_3P/NF. Advanced analyses (X-ray photoelectron spectroscopy (XPS), zeta potential analysis, and ultraviolet photoelectron spectroscopy (UPS)) revealed that higher crystallinity improved charge redistribution, accelerated charge accumulation, and enhanced intermediate adsorption, thereby boosting OER performance. The catalyst achieved low overpotentials of 281 mV (50 mA cm^{-2}) and 306 mV (100 mA cm^{-2}), demonstrating exceptional stability and outperforming comparable systems and noble metal catalysts. *In situ* studies revealed the rapid formation of active CoOOH phases on MnP–$Co_3(PO_4)_2$/NF, surpassing its low-crystallinity counterpart. This work provides a strategic approach to phase engineering, advancing the design of efficient and stable OER catalysts for energy conversion applications.

2. Experimental sections

2.1. Materials

Manganese(II) acetate tetrahydrate ($Mn(CH_3COO)_2{\cdot}4H_2O$, 99%, Aladdin, 500 g), cobaltous(II) nitrate hexahydrate ($Co(CH_3COO)_2{\cdot}6H_2O$, 99.5%, Aladdin, 100 g), urea ($CO(NH_2)_2$, 99.0%, Aladdin, 500 g), ammonium fluoride (NH_4F, 96.0%, Aladdin, 500 g), sodium hypophosphite monohydrate ($NaH_2PO_2{\cdot}H_2O$, ≥99%, Xilong Scientific, 500 g), potassium hydroxide (KOH, AR, >90%, Macklin, 500 g), ethanol (C_2H_5OH, AR, 99.5%, Xilong Scientific, 500 mL), Nafion (5 wt%, Alfa Aesar, 100 mL), Pt/C (20 wt% Pt, Alfa Aesar, 1 g), and nickel foam (NF) as a substrate (Suzhou Sinero Technology Co, Ltd, with a thickness of 1.6 mm) were used. RuO_2 powder was prepared by directly annealing $RuCl_3{\cdot}3H_2O$ (37%, Inno-chem, 25 g) at 400 °C in air. All reagents were commercially available and could be used directly without further purification.

2.2. Synthesis of $CoMnO_3$–MnO(OH)/NF

A 1.5 cm × 3.5 cm piece of nickel foam (NF) was ultrasonically cleaned sequentially in 0.5 M H_2SO_4, ethanol, and deionized water for 15 minutes each to ensure the removal of surface impurities. Subsequently, 1.0 mmol of $Co(CH_3COO)_2{\cdot}6H_2O$, 2.0 mmol of $Mn(CH_3COO)_2{\cdot}4H_2O$, 4.0 mmol of NH_4F, and 4.5 mmol of $CO(NH_2)_2$ were dissolved in 50 mL of deionized water to form a uniform solution under magnetic stirring at room temperature. The treated NF was immersed in the solution and transferred into a 100 mL Teflon-lined stainless-steel autoclave. The autoclave was heated at 120 °C for 7 h and then cooled naturally to room temperature. The resulting product, $CoMnO_3$–MnO(OH)/NF, was washed several times with ethanol and deionized water and then dried at 60 °C for 3 h.

2.3. Synthesis of $CoMnO_3$–$CoCo_2O_4$/NF

The pre-prepared $CoMnO_3$–MnO(OH)/NF was placed in the tube furnace and gradually heated to 400 °C at a rate of 5 °C min^{-1} for 120 min under a nitrogen atmosphere to obtain $CoMnO_3$–$CoCo_2O_4$/NF.

2.4. Synthesis of MnP–$Co_3(PO_4)_2$/NF

$NaH_2PO_2{\cdot}H_2O$ (1.0 g) and pre-prepared $CoMnO_3$–$CoCo_2O_4$/NF were, respectively, placed upstream and downstream of the same tube furnace. The tube furnace was slowly heated to 350 °C for 120 minutes with a heating rate of 5 °C min^{-1} under a N_2 atmosphere to obtain MnP–$Co_3(PO_4)_2$/NF.

A series of samples with varying Co/Mn ratios (3/0, 2.5/0.5, 1.5/1.5, 1/2, and 0/3) were prepared at different hydrothermal synthesis temperatures (100 °C, 140 °C, 160 °C, and 180 °C) using a consistent synthesis method.

2.5. Synthesis of MnP–Co_3P/NF

For comparison, MnP–Co_3P/NF was synthesized *via* direct phosphation of the $CoMnO_3$–MnO(OH)/NF precursor with $NaH_2PO_2{\cdot}H_2O$ at 350 °C for 2 h, omitting a prior 400 °C heat treatment step.

2.6. Synthesis of RuO_2/NF and 20 wt% Pt/C/NF electrodes

To prepare the catalyst ink, 2 mg of RuO_2 and 20 wt% Pt/C were dispersed in a mixture of 200 μL of deionized water, 200 μL of ethanol, and 10 μL of 5 wt% Nafion solution. The suspension was ultrasonicated for 30 minutes, and then drop-cast onto a pristine NF substrate (1 cm × 1 cm) and dried under ambient conditions.

3. Results and discussion

3.1. Synthesis and characterization studies

The synthesis of MnP–$Co_3(PO_4)_2$/NF followed the schematic in Fig. 1a. Low-crystallinity metal hydroxides ($CoMnO_3$–MnO(OH)/NF) were first prepared *via* a hydrothermal process and subsequently annealed under an inert atmosphere to form crystalline oxides ($CoMnO_3$–$CoCo_2O_4$/NF), as shown in Fig. S2a and b.† These oxides were then phosphorized to produce crystalline MnP–$Co_3(PO_4)_2$/NF. For comparison, MnP–Co_3P/NF was synthesized without annealing. XRD analysis (Fig. 1b and c) confirmed the low crystallinity of MnP–Co_3P/NF, while $Co_3(PO_4)_2$/NF and $Mn(P_3O_9)$–Mn_2O_3/NF, derived from Co- or Mn-exclusive precursors, were also characterized (Fig. S3a and b†). This systematic approach highlights the role of annealing in crystallinity control and phase evolution. N_2 adsorption/desorption isotherms were employed to further investigate the structural properties to determine the Brunauer–Emmett–Teller (BET) surface area and pore structures of the catalysts. MnP–$Co_3(PO_4)_2$/NF exhibited a higher specific surface area (4.8121 m^2 g^{-1}) compared to MnP–Co_3P/NF (2.1662 m^2 g^{-1}) (Fig. S4a and b†), emphasizing the role of annealing in increasing active site exposure and facilitating mass transport.[30] Barrett–Joyner–Halenda (BJH) analysis confirmed the mesoporous structure, with an average pore width of 39.641 nm (Fig. S4a–d†). The combined annealing and phosphating processes promoted mesopore formation, increasing surface area and creating efficient transport channels, which are critical for optimizing electrocatalytic performance.[1]

Furthermore, the MnP–$Co_3(PO_4)_2$/NF exhibited superhydrophilicity, with a static contact angle (CA) of zero, enabling instant water permeation (Fig. 1d); in contrast, MnP–Co_3P/NF exhibited a CA of 55.3°. This property enhances mass transport and electrolyte–active site interaction, improving catalytic efficiency.[31] Electron paramagnetic resonance (EPR) spectroscopy further confirmed phosphorus vacancies in the phosphide samples, with sharp peaks at g = 2.002, absent in $CoMnO_3$–MnO(OH)/NF and $CoMnO_3$–$CoCo_2O_4$/NF.[32,33] MnP–$Co_3(PO_4)_2$/NF exhibited stronger EPR signals (Fig. 1e, inset), indicating a higher phosphorus vacancy concentration, facilitated by its crystalline oxide structure. These vacancies are expected to optimize electron distribution, expose additional active sites, and accelerate reaction kinetics, collectively enhancing electrocatalytic performance.[34]

Transmission electron microscopy (TEM) and scanning electron microscopy (SEM) analyses were used to study the morphological and crystallographic differences between MnP–$Co_3(PO_4)_2$/NF and MnP–Co_3P/NF. The precursor $CoMnO_3$–MnO(OH)/NF exhibited a nanowire morphology (Fig. 2a), which transformed into unfurling nanoflowers ($CoMnO_3$–$CoCo_2O_4$/NF) upon annealing at 400 °C (Fig. 2b). This nanoflower structure was retained in MnP–$Co_3(PO_4)_2$/NF post-phosphorization (Fig. 2c). At the same time, MnP–Co_3P/NF maintained the nanowire structure without annealing (Fig. 2d). The nanoflower architecture enhanced electrolyte penetration, improved oxygen diffusion, and increased active site density. In contrast, $Co_3(PO_4)_2$/NF showed formation of dense petal-like structures (Fig. S5a†), and $Mn(P_3O_9)$–Mn_2O_3/NF featured dense, blocky particles (Fig. S5b†). These morphological distinctions highlight the role of annealing in modulating structure and crystallinity, directly impacting electrocatalytic efficiency. Additionally, systematic variations in the Co/Mn ratios and hydrothermal temperatures modulated the morphology of CoMn–X–Y/NF (Fig. S6a–c and S7a–d†), offering a pathway for catalyst optimization.

TEM analysis revealed that MnP–$Co_3(PO_4)_2$/NF exhibits a well-defined nanosheet structure with distinct lattice fringes (0.280 nm for the $Co_3(PO_4)_2$ (220) plane and 0.263 nm for the MnP (200) plane) and clear SAED diffraction spots (Fig. 2e–g), confirming high crystallinity. In contrast, MnP–Co_3P/NF showed lower crystallinity, with faint lattice streaks and diffuse SAED rings (Fig. 2h and i). High-angle annular dark-field scanning transmission electron microscopy (HAADF-STEM) and elemental mapping (Fig. 2j–n) demonstrated uniform distribution of Co, Mn, O, and P in MnP–$Co_3(PO_4)_2$/NF, supported by energy-dispersive X-ray spectroscopy (EDX) (Fig. S8†). These results highlight the enhanced crystallinity and structural integrity of MnP–$Co_3(PO_4)_2$/NF, emphasizing the role of annealing and phosphating in optimizing crystallographic properties for enhanced electrocatalytic performance.

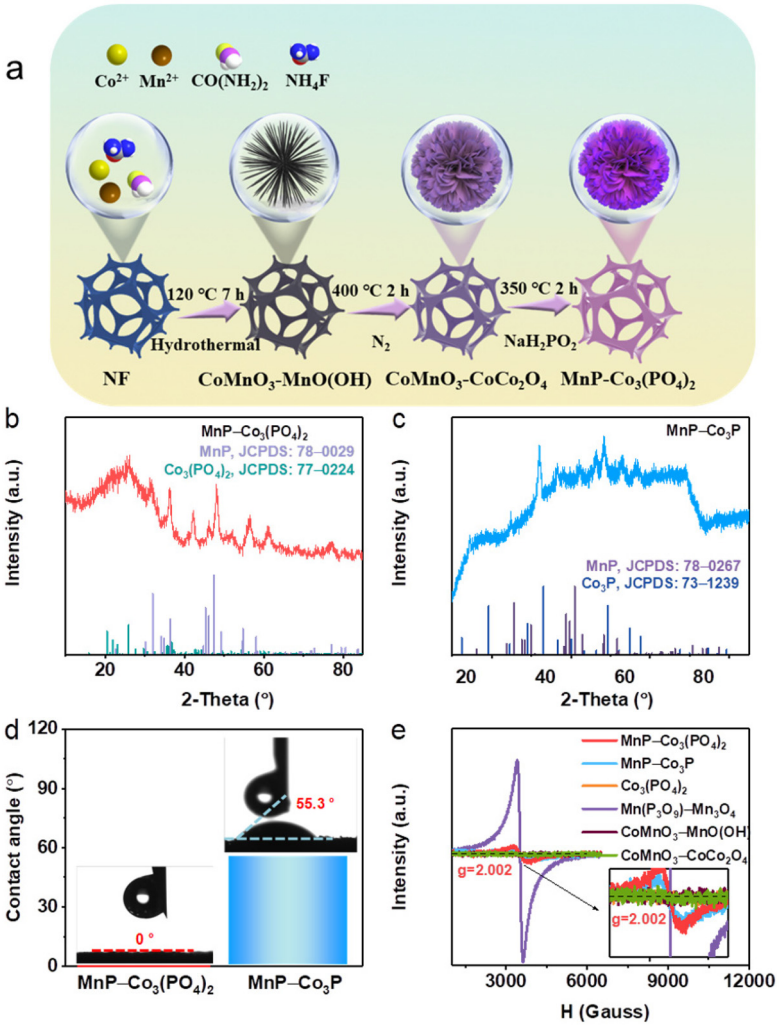

Fig. 1 (a) Schematic illustration of the synthesis of MnP–$Co_3(PO_4)_2$/NF. XRD patterns of (b) MnP–$Co_3(PO_4)_2$/NF and (c) MnP–Co_3P/NF. (d) The contact angle test for MnP–$Co_3(PO_4)_2$/NF and MnP–Co_3P/NF. (e) Electron paramagnetic resonance (EPR) spectra of the different catalysts.

XPS depth profiling elucidated the samples' chemical states and structural properties. The survey spectrum of MnP–$Co_3(PO_4)_2$/NF (Fig. S9a†) confirmed the presence of Co, Mn, O, and P, with C 1s at 284.0 eV as a reference (Fig. S9b†). The Co 2p spectrum (Fig. 3a) was deconvoluted into peaks corresponding to Co^{3+} (780.49 eV), Co^{2+} (781.97 eV), Co–P (777.95 eV), and satellite peaks (785.73 eV).[35] MnP–$Co_3(PO_4)_2$/NF exhibited a 0.42 eV negative shift in Co 2p binding energy compared to $Co_3(PO_4)_2$/NF, while MnP–Co_3P/NF showed only a 0.09 eV shift. This suggests that Mn incorporation effectively reduces the electron density of Co cations, facilitating electron transfer and enhancing OER performance.[36,37] The Mn 2p spectrum (Fig. 3b) revealed Mn–P bonding at 637.21 eV (consistent with XRD and TEM results),[38] and peaks for Mn^{2+} (641.03 eV), Mn^{3+} (644.45 eV), and Mn^{4+} (646.97 eV).[39] MnP–$Co_3(PO_4)_2$/NF showed a 0.30 eV positive shift, while MnP–Co_3P/NF exhibited a more pronounced 0.49 eV shift, indicating that crystallinity plays a critical role in Mn charge transfer. Electron transfer between Mn and Co optimizes the binding energy, optimizing the adsorption of reaction intermediates and enhancing OER activity.[37,40] In the P 2p spectrum (Fig. 3c), peaks at 128.79 eV and 129.74 eV correspond to P $2p_{3/2}$ and P $2p_{1/2}$, indicating metal–P bonds,[41] while the peak at 133.45 eV is attributed to P–O bonds resulting from surface oxidation.[42] The lower P $2p_{3/2}$ binding energy in MnP–$Co_3(PO_4)_2$/NF indicates the presence of phosphorus vacancies, consistent with the EPR data (Fig. 1e).[43] These results demonstrate strong electronic interactions and structural reconfiguration in the catalyst, driven by Co and Mn incorporation, which collectively optimize the electronic environment and enhance the catalytic performance of the material.[44]

Zeta potential (ζ) measurements revealed that MnP–$Co_3(PO_4)_2$/NF exhibits a more negative value (−24.63 mV) compared to MnP–Co_3P/NF (−19.70 mV), $Co_3(PO_4)_2$/NF (−19.77 mV), and $Mn(P_3O_9)$–Mn_2O_3/NF (2.04 mV) in a KOH electrolyte. This more negative ζ potential suggests an increased OH^- concentration in the inner Helmholtz layer, promoting rapid charge accumulation and enhancing OER

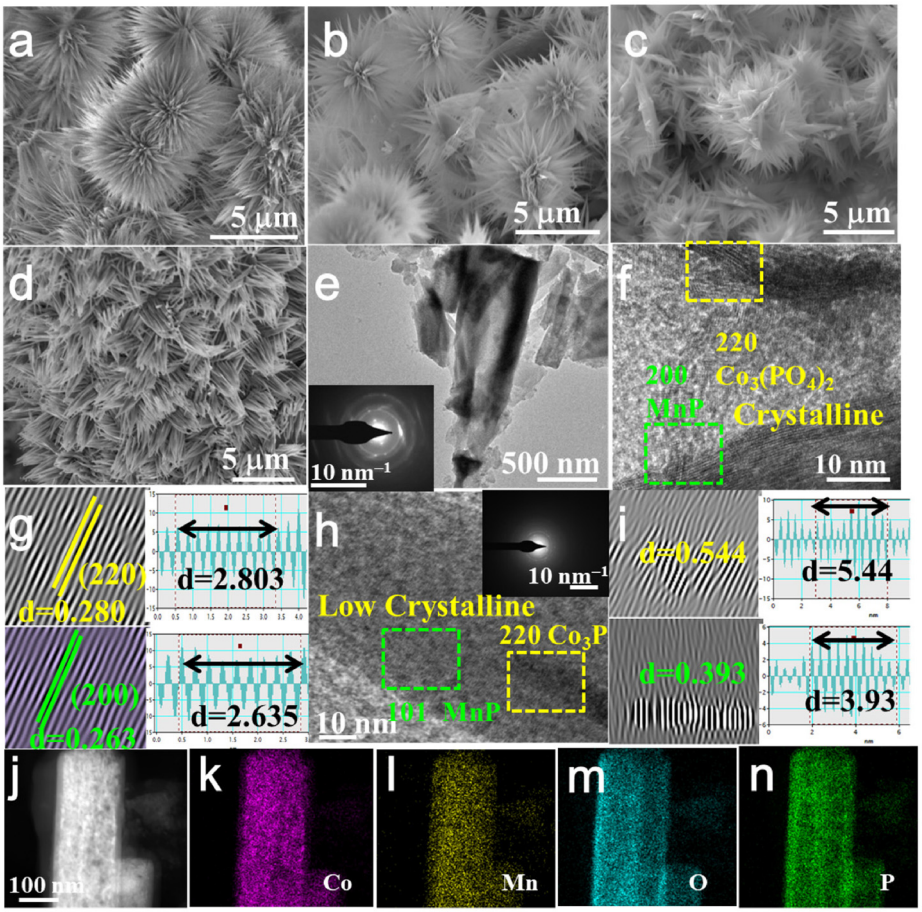

Fig. 2 SEM images of (a) $CoMnO_3$–MnO(OH)/NF, (b) $CoMnO_3$–$CoCo_2O_4$/NF, (c) MnP–$Co_3(PO_4)_2$/NF and (d) MnP–Co_3P/NF. (e) TEM image/SAED image (inset), (f) HR-TEM image, and (g) the intensity profile of corresponding areas of the MnP–$Co_3(PO_4)_2$/NF. (h) HR-TEM image/SAED image (inset) and (i) the intensity profile of corresponding areas of the MnP–Co_3P/NF. (j) HAADF-STEM image and (k–n) elemental mappings (Co, Mn, O, and P) of the MnP–$Co_3(PO_4)_2$/NF.

efficiency in alkaline media. These results highlight the importance of surface charge modulation in optimizing catalytic performance (Fig. 3d).[45,46] The work function (WF), calculated as WF = 21.22 eV − E_{cutoff},[44,47] followed the trend MnP–$Co_3(PO_4)_2$/NF (2.90 eV) < MnP–Co_3P/NF (3.32 eV) < $CoMnO_3$–$CoCo_2O_4$/NF (6.82 eV) < $CoMnO_3$–MnO(OH)/NF (7.05 eV) (Fig. 3e and f, S10†). The lower WF of MnP–$Co_3(PO_4)_2$/NF indicates enhanced electron mobility from bulk to surface, improving charge redistribution and reaction kinetics.[48] Additionally, its valence band maximum (1.34 eV) was lower than those of MnP–Co_3P/NF (3.17 eV) and $CoMnO_3$–MnO(OH)/NF (1.37 eV), indicating a shift toward the Fermi level and an increase in empty antibonding states, which enhance intermediate adsorption. These electronic modifications increase conductivity and catalytic performance, highlighting the impact of coordination engineering in optimizing electrocatalysts.[49]

3.2. Electrocatalytic performance

The OER activity of the catalysts was evaluated in 1 M KOH using a three-electrode system, with *iR*-corrected potentials referenced to the RHE (Fig. S1†). LSV curves (Fig. 4a) show that MnP–$Co_3(PO_4)_2$/NF achieves overpotentials of 281 mV (50 mA cm^{-2}) and 306 mV (100 mA cm^{-2}), outperforming MnP–Co_3P/NF, $Co_3(PO_4)_2$/NF, $Mn(P_3O_9)$–Mn_2O_3/NF, and RuO_2 (Fig. 4c). These results highlight the importance of coordinated annealing in balancing the amorphous and crystalline phases, thereby enhancing OER performance. This study emphasizes the importance of phase engineering in designing efficient electrocatalysts for energy conversion. Tafel slope analysis confirms that MnP–$Co_3(PO_4)_2$/NF exhibits enhanced OER kinetics with a low value of 76.84 mV dec^{-1} (Fig. 4b). CV measurements (Fig. S11a–f†) reveal its high C_{dl} (254.9 mF cm^{-2}), indicating abundant active sites and the largest electrochemical surface area (ECSA) (Fig. 4d and e).[50] MnP–$Co_3(PO_4)_2$/NF outperforms recently reported catalysts (Fig. 4f, Table S1†) and shows the lowest charge transfer resistance in EIS analysis (Fig. 4g), highlighting its superior conductivity and charge transfer. These results demonstrate the exceptional OER performance of MnP–$Co_3(PO_4)_2$/NF, driven by optimized structural and electronic properties.[51]

Systematic optimization identified MnP–$Co_3(PO_4)_2$/NF as the most active OER catalyst at a hydrothermal temperature of

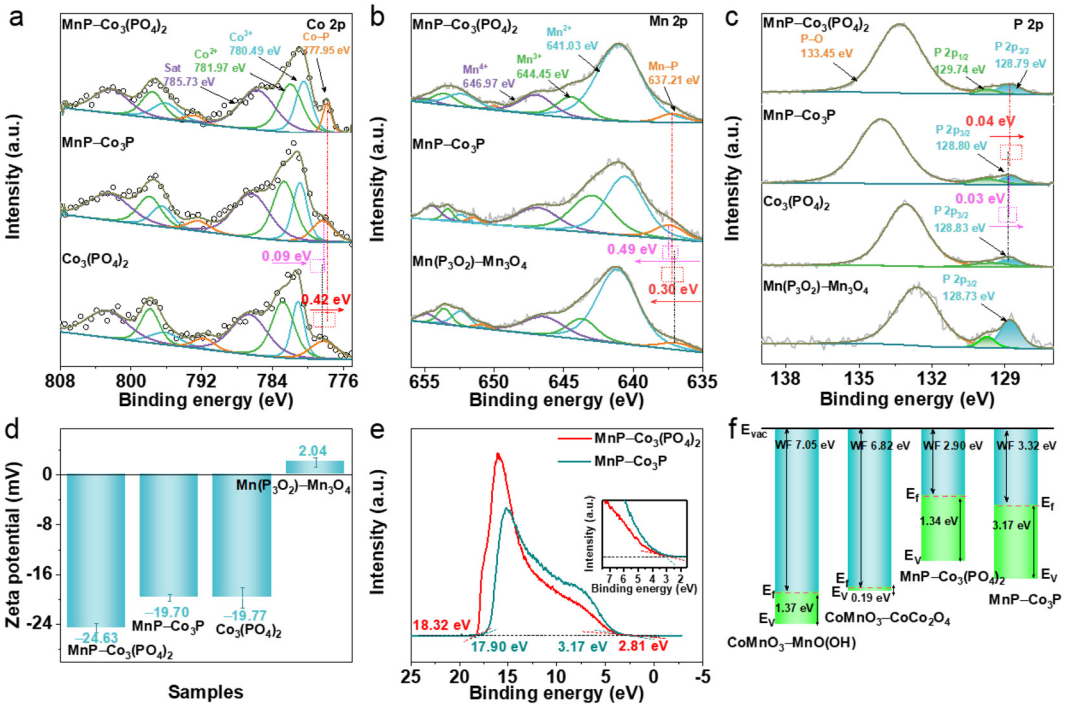

Fig. 3 High resolution XPS spectra of (a) Co 2p, (b) Mn 2p, and (c) P 2p of designed catalysts. (d) Zeta potentials of designed catalysts in KOH. (e) UPS spectra and (f) band structure alignment of the designed catalysts.

120 °C and a Co/Mn molar ratio of 2 : 1 (Fig. S12–S15†), leveraging synergistic effects from precise temperature and compositional control. The stability test was performed in a standard three-electrode system, in which the catalyst, graphite plate, and saturated calomel electrode (SCE) were used as the working, counter, and reference electrodes, respectively. Chronoamperometric tests demonstrated exceptional stability, maintaining consistent performance over 420 h at 10 mA cm^{-2} (Fig. 4h). At 100 mA cm^{-2}, MnP–Co_3P/NF showed a 21% decrease in current density after 70 h, while MnP–$Co_3(PO_4)_2$/NF exhibited only an 11% reduction. This superior stability stems from the balance between amorphous and crystalline structures achieved through annealing and phosphating, enhancing both catalytic activity and durability.

3.3. Dynamic transformation analysis

Operando electrochemical impedance spectroscopy (EIS) tests were employed to investigate the interfacial charge transfer dynamics of MnP–$Co_3(PO_4)_2$/NF and MnP–Co_3P/NF during the OER. Bode plots identified two regions: high frequencies for electron transfer within the catalyst's inner layer and low frequencies for charge transfer at the catalyst/electrolyte interface (Fig. 5a and b, S16a and b†).[52] Below 1.35 V (*vs.* RHE), neither catalyst showed phase angle arching due to high interfacial resistance. At 1.4 V, both catalysts exhibited phase angle arching, indicating charge transfer initiation. MnP–$Co_3(PO_4)_2$/NF exhibited a smaller phase angle, suggesting faster intermediate oxidation and *OOH deprotonation. From 1.35 to 1.50 V, although the peak phase angles decreased for both catalysts, MnP–$Co_3(PO_4)_2$/NF consistently showed lower values, demonstrating more efficient interfacial charge transfer (Fig. 5c). These results highlight MnP–$Co_3(PO_4)_2$/NF's superior charge transfer dynamics, contributing to its enhanced OER performance. *In situ* Raman spectroscopy was used to monitor the structural evolution and elucidate the OER mechanism.[53] For MnP–$Co_3(PO_4)_2$/NF (Fig. 5d), the CoOOH peak at 628 cm^{-1} appeared at 1.30 V (*vs.* RHE), indicating easier CoOOH formation. In contrast, CoOOH species only emerged at potentials above 1.40 V for MnP–Co_3P/NF (Fig. 5e). A lower onset potential for the OER intermediate CoOOH suggests that MnP–$Co_3(PO_4)_2$/NF exhibits higher catalytic efficiency.[54]

CV measurements were performed to investigate valence state changes of active species during the OER.[55] After 10 preconditioning cycles at 50 mV s^{-1}, the steady-state CV curve (Fig. 5f) revealed that electrons migrated to the NF electrode and holes oxidized Co^{2+} to Co^{3+}.[15] For MnP–$Co_3(PO_4)_2$/NF, the Co^{2+}/Co^{3+} redox transition occurred at ~1.50 V, whereas for MnP–Co_3P/NF, it was observed at ~1.55 V. This lower oxidation potential for MnP–$Co_3(PO_4)_2$/NF indicates easier oxidation, enhancing surface remodeling and accelerating OER kinetics.[18]

In situ Fourier-transform infrared (ATR FTIR) spectroscopy, using a custom electrochemical setup, was employed to study OER intermediates and the catalytic mechanism, leveraging its high sensitivity towards oxygen-containing species.[56,57] For MnP–$Co_3(PO_4)_2$/NF, absorption bands at 1181 cm^{-1} (OOH*), 3476 cm^{-1} (OH*), and 1634 cm^{-1} (H–O–H bending) appeared at 1.05 V (Fig. 5g). The OH* intensity increased with the poten-

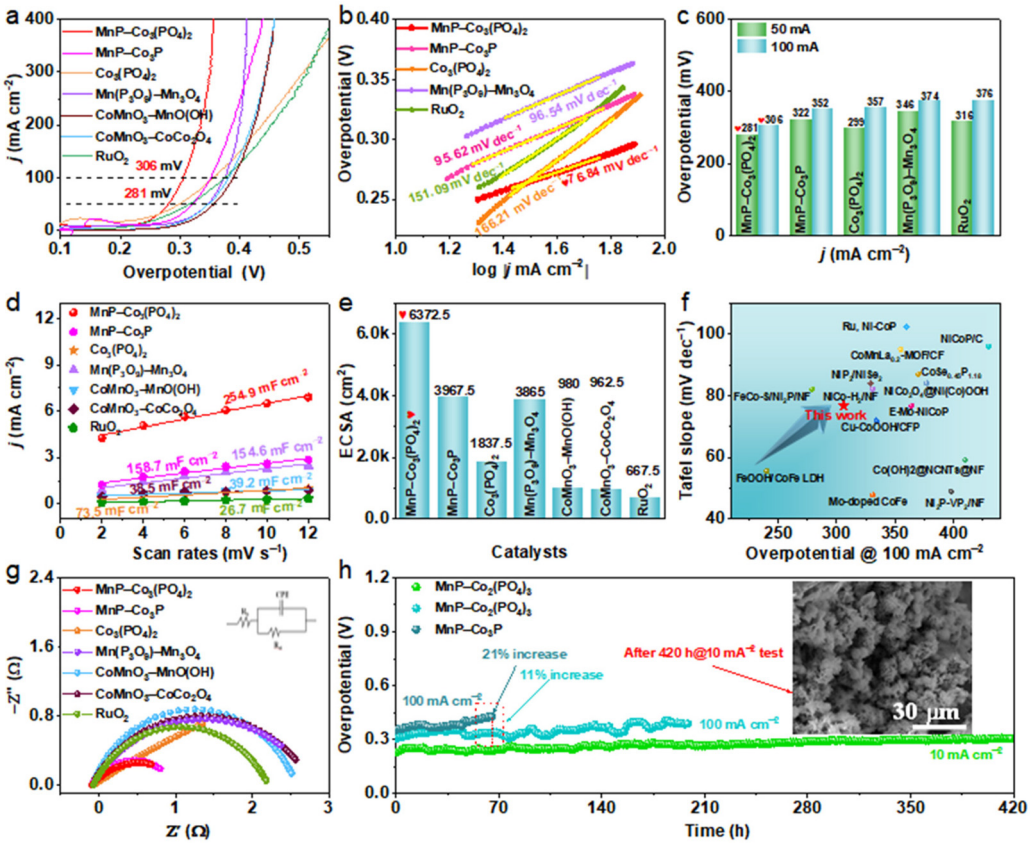

Fig. 4 (a) LSV polarization curves, (b) Tafel slopes, (c) summary of overpotentials (at 50 and 100 mA cm^{-2}) in 1.0 M KOH, (d) C_{dl} and (e) summary of ECSA of the designed catalysts. (f) Comparison of overpotentials (at 100 mA cm^{-2}) and Tafel slopes for various state-of-the-art OER catalysts. (g) Electrochemical impedance spectroscopy of prepared catalysts. (h) Chronopotentiometry of MnP–$Co_3(PO_4)_2$/NF (at 10 and 100 mA cm^{-2}) and MnP–Co_3P/NF (at 100 mA cm^{-2}) (the inset shows the morphology of MnP–$Co_3(PO_4)_2$/NF after stability at 10 mA cm^{-2}).

tial, indicating accelerated kinetics due to OH* accumulation.[58] The H–O–H peak at lower potentials highlighted rapid reaction initiation and efficient water participation,[59] while MnP–Co_3P/NF (Fig. 5h) required 1.20 V to generate similar peaks, suggesting higher energy demands. The OOH* peak at 1181 cm^{-1} emerged earlier for MnP–$Co_3(PO_4)_2$/NF (1.05 V) than for MnP–Co_3P/NF, with its intensity increasing more significantly with potential (Fig. 5i).[60] This demonstrates faster OOH* formation on MnP–$Co_3(PO_4)_2$/NF.[61]

Post-OER HR-TEM analysis (Fig. S17†) unambiguously demonstrates the *in situ* formation of crystalline CoOOH (*d*-spacing = 0.211 nm, corresponding to the (012) plane), which is widely recognized as the true active phase for the OER in cobalt-based catalysts. This structural transformation is particularly advantageous because the layered CoOOH structure facilitates OH^- intercalation and promotes the formation of highly active Co sites during the OER, while the well-defined crystalline domains maintain structural integrity during prolonged electrocatalysis.[62] The post-OER XPS analysis (Fig. S18a, b and d†) reveals notable changes in oxidation states: (1) the Co^{3+}/Co^{2+} ratio increases from 0.74 to 1.69, generating electron-deficient Co centers that promote OH^- attack and optimize e_g orbital filling for metal–oxo bond formation; and (2) the Mn^{3+}/Mn^{2+} ratio rises from 0.18 to 1.51, enhancing Jahn–Teller distortion for stronger oxygen binding, while the reduced Mn^{4+}/Mn^{3+} ratio (from 1.04 to 0.72) ensures redox flexibility without over-oxidation.[16,63] The disappearance of the P–M peak (Fig. S18c†) confirms oxidation of phosphorus to phosphate species, indicating surface chemical reconstruction associated with enhanced OER performance.

3.4. Overall water splitting performance

The OER performance of MnP–$Co_3(PO_4)_2$/NF was evaluated in an industrial alkaline electrolyzer using a two-electrode configuration with a Pt/C cathode (Fig. 6a). The MnP–$Co_3(PO_4)_2$/$NF^{(+)}$||$Pt/C^{(-)}$ system outperformed the commercial $RuO_2^{(+)}$||$Pt/C^{(-)}$ electrolyzer, achieving current densities of 200–1000 mA cm^{-2} at lower cell voltages (1.80–2.02 V) (Fig. 6b and c). It also demonstrated exceptional stability, maintaining consistent performance for 230 h at 100 mA cm^{-2} (Fig. 6e), surpassing the RuO_2-based system. Additionally, MnP–$Co_3(PO_4)_2$/$NF^{(+)}$||$Pt/C^{(-)}$ outperformed most reported noble metal-free catalysts at 10 mA cm^{-2} (Fig. 6d, S2†). The MnP–$Co_3(PO_4)_2$/$NF^{(+)}$||$Pt/C^{(-)}$ electrolyzer efficiently operates at low voltages using a 1.5 V AA battery or solar cell (Fig. 6f). Visible H_2 and O_2 bubble evolution confirms its capability for overall water splitting with

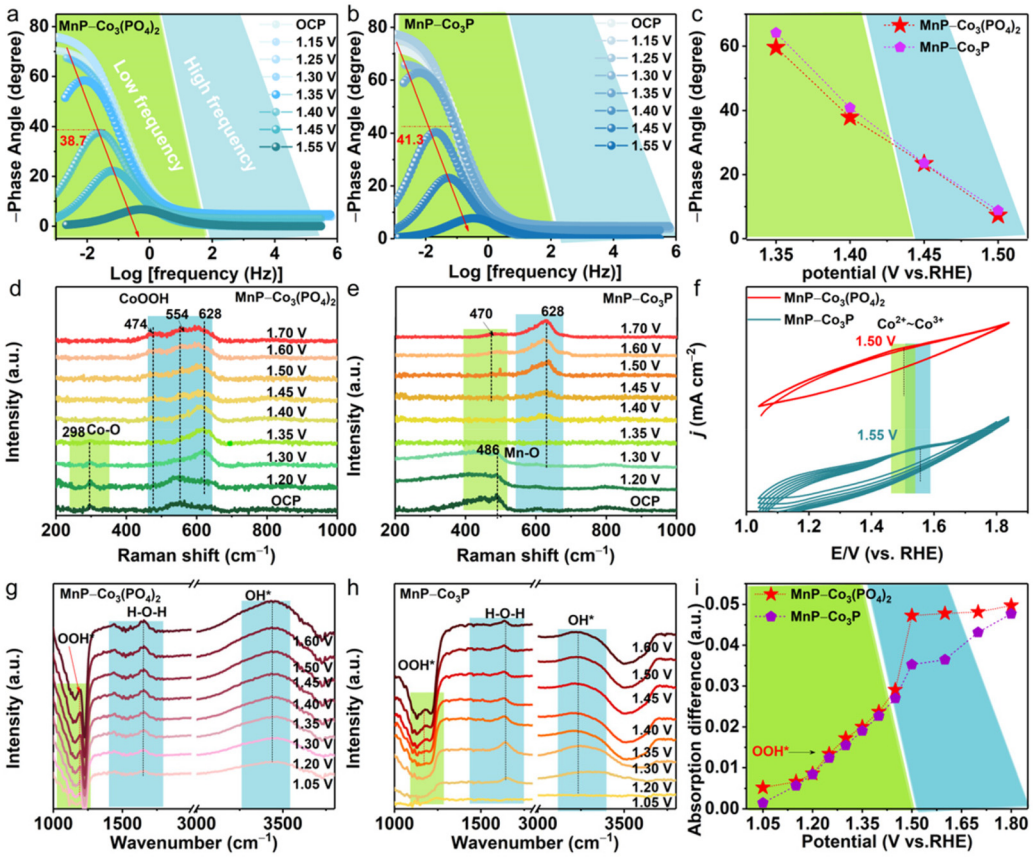

Fig. 5 Bode phase plots of (a) MnP–$Co_3(PO_4)_2$/NF and (b) MnP–Co_3P/NF at various potentials. (c) The peak phase angles of MnP–$Co_3(PO_4)_2$/NF and MnP–Co_3P/NF at 1.35–1.5 V. (*vs.* RHE). Electrochemical *in situ* Raman spectra of (d) MnP–$Co_3(PO_4)_2$/NF and (e) MnP–Co_3P/NF in the potential range of 0–1.70 V (*vs.* RHE). (f) Cyclic voltammograms of the Co^{2+}/Co^{3+} redox peak for the designed catalysts, showing Co^{2+} to Co^{3+} transition, measured over 10 cycles at 50 mV s^{-1}. *In situ* ATR FTIR spectra of (g) MnP–$Co_3(PO_4)_2$/NF, (h) MnP–Co_3P/NF and (i) intensity differences of the infrared signals at OOH* as a function of potential for MnP–$Co_3(PO_4)_2$/NF and MnP–Co_3P/NF electrocatalysts during the OER process.

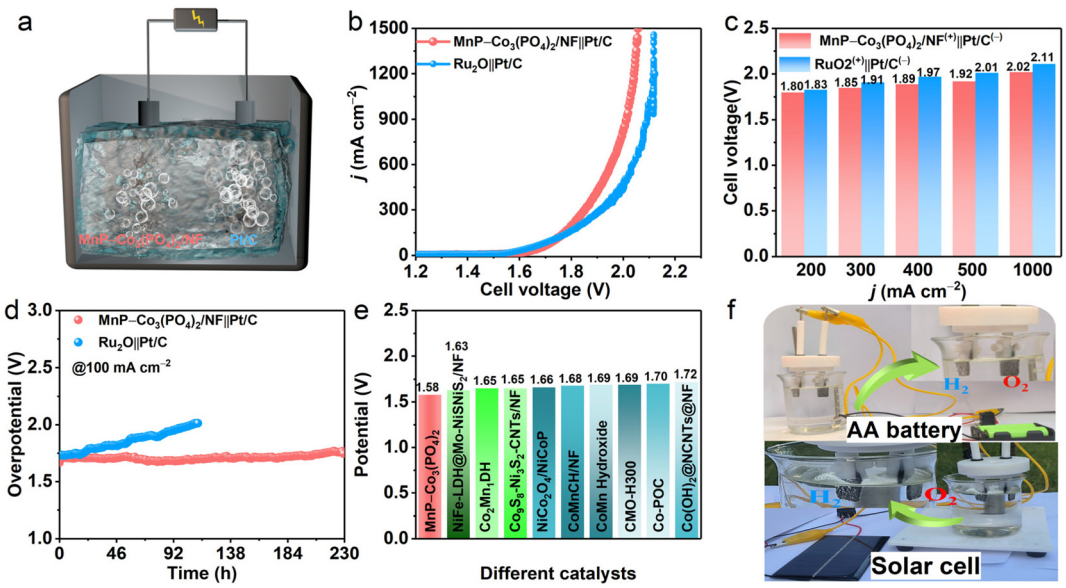

Fig. 6 (a) Schematic representation of the electrolyzer for overall water splitting in a two-electrode system. (b) LSV curves of overall water splitting for MnP–$Co_3(PO_4)_2$/$NF^{(+)}$||$Pt/C^{(-)}$ and $RuO_2{}^{(+)}$||$Pt/C^{(-)}$ in 1.0 M KOH. (c) Comparison of the required voltages at different current densities. (d) Chronopotentiometry curves of MnP–$Co_3(PO_4)_2$/$NF^{(+)}$||$Pt/C^{(-)}$ and $RuO_2{}^{(+)}$||$Pt/C^{(-)}$ electrolyzers at 100 mA cm^{-2}. (e) Comparison of cell voltage at 10 mA cm^{-2} for MnP–$Co_3(PO_4)_2$/NF relative to recently reported catalysts. (f) Diagram of practical water splitting operation driven by a single AA battery and solar cell.

diverse energy sources. This adaptability to renewable energy systems highlights the practical versatility and industrial scalability of the MnP–$Co_3(PO_4)_2$/NF anode for large-scale renewable energy applications.

Our catalyst shows excellent OER activity and stability, enabling green hydrogen production by replacing expensive IrO_2/RuO_2 in alkaline electrolyzers. It can also be integrated with CO_2 and N_2 reduction for renewable energy storage while improving the efficiency of Zn–air and Li–O_2 batteries. Fabricated *via* a scalable low-temperature hydrothermal process, its non-precious metal composition reduces material costs to less than 5% of RuO_2. Pilot tests in MEAs are currently underway with industry partners under real-world conditions.

4. Conclusion

In this study, annealing before phosphating effectively balanced amorphous and crystalline phases in Co–Mn phosphates, yielding highly crystalline MnP–$Co_3(PO_4)_2$/NF, as confirmed by XRD, SAED, and HR-TEM. Compared to MnP–Co_3P/NF, MnP–$Co_3(PO_4)_2$/NF exhibited enhanced hydrophilicity, higher oxygen vacancy density, and a larger surface area. XPS, zeta potential, and UPS analyses revealed improved charge redistribution, faster charge accumulation, and enhanced intermediate adsorption, collectively boosting the OER performance. MnP–$Co_3(PO_4)_2$/NF achieved low overpotentials of 281 mV (50 mA cm^{-2}) and 306 mV (100 mA cm^{-2}), with exceptional stability, outperforming similar systems and commercial noble metal catalysts. *In situ* studies confirmed faster CoOOH formation on MnP–$Co_3(PO_4)_2$/NF, further enhancing catalytic activity. This work introduces annealing as a strategy for crystallinity control, offering a novel approach for designing efficient and durable OER catalysts.

Author contributions

Tingting Tang: writing – original draft, data curation, and conceptualization. Yanfang Teng: methodology and data curation. Kuoteng Sun: investigation. Yanhan Liu: formal analysis. Zhendong Gao: investigation. Tayirjan Taylor Isimjan: writing – review & editing. Jingya Guo: writing – review & editing. Jianniao Tian: writing – review & editing. Xiulin Yang: writing – review & editing, supervision, and funding acquisition.

Conflicts of interest

There are no conflicts to declare.

Data availability

The data supporting this article have been included as part of the ESI.†

Acknowledgements

This work has been supported by the National Natural Science Foundation of China (no. 52363028, 21965005), the Natural Science Foundation of Guangxi Province (2021GXNSFAA076001 and 2018GXNSFAA294077), and the Guangxi Technology Base and Talent Subject (GUIKE AD23023004 and GUIKE AD20297039).

References

1 L. Li, X. Zhang, M. Humayun, X. Xu, Z. Shang, Z. Li, M. F. Yuen, C. Hong, Z. Chen, J. Zeng, M. Bououdina, K. Temst, X. Wang and C. Wang, *ACS Nano*, 2024, **18**, 1214–1225.
2 H. Zhang, X. Huang and Y. Chen, *Chem. Rev.*, 2024, **124**, 245–247.
3 R. Gao and D. Yan, *Adv. Energy Mater.*, 2020, **10**, 1900954.
4 H. Su, J. Jiang, N. Li, Y. Gao and L. Ge, *Chem. Eng. J.*, 2022, **446**, 137226.
5 Y. Pan, J. Gao, E. Lv, T. Li, H. Xu, L. Sun, A. Nairan and Q. Zhang, *Adv. Funct. Mater.*, 2023, **33**, 2303833.
6 U. Khan, A. Nairan, J. Gao and Q. Zhang, *Small Struct.*, 2023, **4**, 2200109.
7 Q. Xue, Z. Wang, Y. Ding, F. Li and Y. Chen, *Chin. J. Catal.*, 2023, **45**, 6–16.
8 X.-L. Liu, Y.-C. Jiang, J.-T. Huang, W. Zhong, B. He, P.-J. Jin and Y. Chen, *Carbon Energy*, 2023, **5**, e367.
9 Y. Yang, S. Wei, Y. Li, D. Guo, H. Liu and L. Liu, *Appl. Catal., B*, 2022, **314**, 121491.
10 G. Mu, H. Xie, Y. Jian, Z. Jiang, L. Li, M. Tian, L. Zhang, J. Wang, S. Chai and C. He, *Sep. Purif. Technol.*, 2024, **348**, 127699.
11 C. Walter, P. W. Menezes, S. Orthmann, J. Schuch, P. Connor, B. Kaiser, M. Lerch and M. Driess, *Angew. Chem., Int. Ed.*, 2018, **57**, 698–702.
12 M. Arif, G. Yasin, M. Shakeel, M. A. Mushtaq, W. Ye, X. Fang, S. Ji and D. Yan, *J. Energy Chem.*, 2021, **58**, 237–246.
13 Z.-X. Ge, Y. Ding, T.-J. Wang, F. Shi, P.-J. Jin, P. Chen, B. He, S.-B. Yin and Y. Chen, *J. Energy Chem.*, 2023, **77**, 209–216.
14 J. Reddy, M. Duraivel, K. Senthil and K. Prabakar, *ChemCatChem*, 2022, **14**, e202200966.
15 N. Kalita, A. Sahu, S. Bhowmick and M. Qureshi, *Chem. Commun.*, 2022, **58**, 13747–13750.
16 J. Li, X. Meng, X. Song, J. Qi, F. Liu, X. Xiao, Y. Du, G. Xu, Z. Jiang, S. Ye, S. Huang and J. Qiu, *Adv. Funct. Mater.*, 2024, **34**, 2316718.
17 H. Xue, A. Meng, T. Yang, Z. Li and C. Chen, *J. Energy Chem.*, 2022, **71**, 639–651.
18 J. Han, H. Wang, Y. Wang, H. Zhang, J. Li, Y. Xia, J. Zhou, Z. Wang, M. Luo, Y. Wang, N. Wang, E. Cortés, Z. Wang, A. Vomiero, Z.-F. Huang, H. Ren, X. Yuan, S. Chen, D. Feng, X. Sun, Y. Liu and H. Liang, *Angew. Chem., Int. Ed.*, 2024, **63**, e202405839.

19 D. Li, H. Baydoun, C. N. Verani and S. L. Brock, *J. Am. Chem. Soc.*, 2016, **138**, 4006–4009.
20 Y. Xu, S. Wei, L. Gan, L. Zhang, F. Wang, Q. Wu, X. Cui and W. Zheng, *Adv. Funct. Mater.*, 2022, **32**, 2112623.
21 P. Zhai, Y. Zhang, Y. Wu, J. Gao, B. Zhang, S. Cao, Y. Zhang, Z. Li, L. Sun and J. Hou, *Nat. Commun.*, 2020, **11**, 5462.
22 X. Ji, Y. Lin, J. Zeng, Z. Ren, Z. Lin, Y. Mu, Y. Qiu and J. Yu, *Nat. Commun.*, 2021, **12**, 1380.
23 H. Han, H. Choi, S. Mhin, Y.-R. Hong, K. M. Kim, J. Kwon, G. Ali, K. Y. Chung, M. Je, H. N. Umh, D.-H. Lim, K. Davey, S.-Z. Qiao, U. Paik and T. Song, *Energy Environ. Sci.*, 2019, **12**, 2443–2454.
24 H. Xu, B. Fei, G. Cai, Y. Ha, J. Liu, H. Jia, J. Zhang, M. Liu and R. Wu, *Adv. Energy Mater.*, 2020, **10**, 1902714.
25 L. Gao, X. Cui, C. D. Sewell, J. Li and Z. Lin, *Chem. Soc. Rev.*, 2021, **50**, 8428–8469.
26 J. Song, C. Wei, Z.-F. Huang, C. Liu, L. Zeng, X. Wang and Z. J. Xu, *Chem. Soc. Rev.*, 2020, **49**, 2196–2214.
27 W. Shao, Y. Xia, X. Luo, L. Bai, J. Zhang, G. Sun, C. Xie, X. Zhang, W. Yan and Y. Xie, *Nano Energy*, 2018, **50**, 717–722.
28 Z.-P. Wu, H. Zhang, S. Zuo, Y. Wang, S. L. Zhang, J. Zhang, S.-Q. Zang and X. W. Lou, *Adv. Mater.*, 2021, **33**, 2103004.
29 H. Xu, C. Wang, G. He, H. Chen and Y. Du, *Inorg. Chem.*, 2022, **61**, 14224–14232.
30 X. Xu, H.-C. Chen, L. Li, M. Humayun, X. Zhang, H. Sun, D. P. Debecker, W. Zhang, L. Dai and C. Wang, *ACS Nano*, 2023, **17**, 10906–10917.
31 L. Yang, X. Cao, X. Wang, Q. Wang and L. Jiao, *Appl. Catal., B*, 2023, **329**, 122551.
32 Y. Gao, K. Wang, C. Xu, H. Fang, H. Yu, H. Zhang, S. Li, C. Li and F. Huang, *Appl. Catal., B*, 2023, **330**, 122627.
33 Y. Yang, L. Shi, Q. Liang, Y. Liu, J. Dong, T. T. Isimjan, B. Wang and X. Yang, *Chin. J. Catal.*, 2024, **56**, 176–187.
34 A. Zhang, Y. Liang, H. Zhang, Z. Geng and J. Zeng, *Chem. Soc. Rev.*, 2021, **50**, 9817–9844.
35 L. Yang, R. Liu and L. Jiao, *Adv. Funct. Mater.*, 2020, **30**, 1909618.
36 K. Ren, W.-J. Xu, K. Li, J.-M. Cao, Z.-Y. Gu, D.-H. Liu, D.-M. Dai, W.-L. Li and X.-L. Wu, *Adv. Funct. Mater.*, 2025, **35**, 2415585.
37 X. Zhao, X. Li, Y. Yan, Y. Xing, S. Lu, L. Zhao, S. Zhou, Z. Peng and J. Zeng, *Appl. Catal., B*, 2018, **236**, 569–575.
38 W. Lu, T. Zheng, X. Zhang, T. He, Y. Sun, S. Li, B. Guan, D. Zhang, Z. Wei, H. Jiang, H. J. Fan and F. Du, *Angew. Chem., Int. Ed.*, 2025, **64**, e202417171.
39 H. Wan, M.-Y. Xie, B. Li, J.-H. Nie, T. Huang, L. Li, J.-H. Shi, M.-H. Xian, J.-R. Huang, W. Hu, G.-F. Huang, F. Gao and W.-Q. Huang, *J. Mater. Sci. Technol.*, 2025, **207**, 1–9.
40 S. Zhao, R. Jin, H. Abroshan, C. Zeng, H. Zhang, S. D. House, E. Gottlieb, H. J. Kim, J. C. Yang and R. Jin, *J. Am. Chem. Soc.*, 2017, **139**, 1077–1080.
41 W. Chen, G. Li, A. Pei, Y. Li, L. Liao, H. Wang, J. Wan, Z. Liang, G. Chen, H. Zhang, J. Wang and Y. Cui, *Nat. Energy*, 2018, **3**, 428–435.
42 M. Li, X. Wang, K. Liu, Z. Zhu, H. Guo, M. Li, H. Du, D. Sun, H. Li, K. Huang, Y. Tang and G. Fu, *Adv. Energy Mater.*, 2023, **13**, 2301162.
43 X. Zhou, H. Gao, Y. Wang, Z. Liu, J. Lin and Y. Ding, *J. Mater. Chem. A*, 2018, **6**, 14939–14948.
44 T. Fang, X. Yu, X. Han, J. Gao and Y. Ma, *Small*, 2024, **20**, 2402478.
45 P. Zhou, X. Lv, S. Tao, J. Wu, H. Wang, X. Wei, T. Wang, B. Zhou, Y. Lu, T. Frauenheim, X. Fu, S. Wang and Y. Zou, *Adv. Mater.*, 2022, **34**, 2204089.
46 M. Xi, Z. Wu, Z. Luo, L. Ling, W. Xu, R. Xiao, H. Wang, Q. Fang, L. Hu, W. Gu and C. Zhu, *Angew. Chem., Int. Ed.*, 2023, **62**, e202302166.
47 C. Lyu, C. Cao, J. Cheng, Y. Yang, K. Wu, J. Wu, W.-M. Lau, P. Qian, N. Wang and J. Zheng, *Chem. Eng. J.*, 2023, **464**, 142538.
48 P. Gayen, S. Saha, K. Bhattacharyya and V. K. Ramani, *ACS Catal.*, 2020, **10**, 7734–7746.
49 Z. Chen, Y. Song, J. Cai, X. Zheng, D. Han, Y. Wu, Y. Zang, S. Niu, Y. Liu, J. Zhu, X. Liu and G. Wang, *Angew. Chem., Int. Ed.*, 2018, **57**, 5076–5080.
50 Y. Zhang, L. Ye, M. Zhang, L. Ma and Y. Gong, *Appl. Surf. Sci.*, 2022, **589**, 152957.
51 S. Niu, T. Tang, Y. Qu, Y. Chen, H. Luo, H. Pan, W.-J. Jiang, J. Zhang and J.-S. Hu, *CCS Chem.*, 2024, **6**, 137–148.
52 X. Zhang, C. Feng, B. Dong, C. Liu and Y. Chai, *Adv. Mater.*, 2023, **35**, 2207066.
53 F. Dionigi, Z. Zeng, I. Sinev, T. Merzdorf, S. Deshpande, M. B. Lopez, S. Kunze, I. Zegkinoglou, H. Sarodnik, D. Fan, A. Bergmann, J. Drnec, J. F. D. Araujo, M. Gliech, D. Teschner, J. Zhu, W.-X. Li, J. Greeley, B. R. Cuenya and P. Strasser, *Nat. Commun.*, 2020, **11**, 2522.
54 Z. Liu, H. Liu, X. Gu and L. Feng, *Chem. Eng. J.*, 2020, **397**, 125500.
55 A. K. Shah, S. Bhowmick, D. Gogoi, N. R. Peela and M. Qureshi, *Chem. Commun.*, 2021, **57**, 8027–8030.
56 H. Su, W. Zhou, H. Zhang, W. Zhou, X. Zhao, Y. Li, M. Liu, W. Cheng and Q. Liu, *J. Am. Chem. Soc.*, 2020, **142**, 12306–12313.
57 H. Su, W. Zhou, W. Zhou, Y. Li, L. Zheng, H. Zhang, M. Liu, X. Zhang, X. Sun, Y. Xu, F. Hu, J. Zhang, T. Hu, Q. Liu and S. Wei, *Nat. Commun.*, 2021, **12**, 6118.
58 W. Zhou, H. Su, Z. Wang, F. Yu, W. Wang, X. Chen and Q. Liu, *J. Mater. Chem. A*, 2021, **9**, 1127–1133.
59 J. Chang, Y. Shi, H. Wu, J. Yu, W. Jing, S. Wang, G. I. N. Waterhouse, Z. Tang and S. Lu, *J. Am. Chem. Soc.*, 2024, **146**, 12958–12968.
60 X. Luo, H. Zhao, X. Tan, S. Lin, K. Yu, X. Mu, Z. Tao, P. Ji and S. Mu, *Nat. Commun.*, 2024, **15**, 8293.
61 M. Zhao, J. Wang, C. Wang, Y. Sun, P. Liu, X. Du, H. Pan, H. Li, H. Liang, J. Guo and T. Ma, *Nano Energy*, 2024, **129**, 110020.
62 S. Cheng, R. Zhang, W. Zhu, W. Ke and E. Li, *Appl. Surf. Sci.*, 2020, **518**, 146106.
63 Y. Zhu, Q. Qian, Y. Chen, X. He, X. Shi, W. Wang, Z. Li, Y. Feng, G. Zhang and F. Cheng, *Adv. Funct. Mater.*, 2023, **33**, 2300547.

